



Defected twisted ring topology for autonomous periodic flip-spin-orbit soft robot

Fangjie Qi^a, Yanbin Li^a, Yaoye Hong^a, Yao Zhao^a, Haitao Qing^a, and Jie Yin^{a,1}

Edited by Renee Zhao, Stanford University, Stanford, CA; received July 24, 2023; accepted November 30, 2023 by Editorial Board Member Yonggang Huang

Periodic spin-orbit motion is ubiquitous in nature, observed from electrons orbiting nuclei to spinning planets orbiting the Sun. Achieving autonomous periodic orbiting motions, along circular and noncircular paths, in soft mobile robotics is crucial for adaptive and intelligent exploration of unknown environments—a grand challenge yet to be accomplished. Here, we report leveraging a closed-loop twisted ring topology with a defect for an autonomous soft robot capable of achieving periodic spin-orbiting motions with programmed circular and re-programmed irregular-shaped trajectories. Constructed by bonding a twisted liquid crystal elastomer ribbon into a closed-loop ring topology, the robot exhibits three coupled periodic self-motions in response to constant temperature or constant light sources: inside-out flipping, self-spinning around the ring center, and self-orbiting around a point outside the ring. The coupled spinning and orbiting motions share the same direction and period. The spinning or orbiting direction depends on the twisting chirality, while the orbital radius and period are determined by the twisted ring geometry and thermal actuation. The flip-spin and orbiting motions arise from the twisted ring topology and a bonding site defect that breaks the force symmetry, respectively. By utilizing the twisting-encoded autonomous flip-spin-orbit motions, we showcase the robot's potential for intelligently mapping the geometric boundaries of unknown confined spaces, including convex shapes like circles, squares, triangles, and pentagons and concaves shapes with multi-robots, as well as health monitoring of unknown confined spaces with boundary damages.

spin-orbit coupling | defect | twisted ring topology | autonomous soft robot | liquid crystal elastomers

Motions observed in nature can be classified into two distinct types: one is non-periodic motions, such as linear motion that moves in a straight line and in one direction (e.g., the path of a laser beam) and irregular motions without fixed patterns (e.g., the flying tack of a fly). The other is periodic motions, such as oscillating or flapping motion (e.g., pistons, waves, pendulums, or flapping wings) and rotary motion (e.g., the spinning and orbiting Earth). Achieving autonomous non-periodic and periodic motions in soft mobile robotics is crucial for adaptive and intelligent exploration of priori unknown environments (1–3). Soft active materials, such as external environmental stimuli-responsive soft materials, hold immense promise for creating autonomous soft robots (1, 4-6). These materials enable the soft robots to autonomously interact with and adapt to the environment without the need for on-board power and control systems, because they can embody self-powering, self-sensing, and self-actuation capabilities in materials, enabling built-in close-looped feedback control known as materials intelligence (7–9).

By combining materials intelligence with different well-designed structures (8), soft active materials-based robots can achieve various autonomous non-periodic (10-20) and periodic motions (21-25) in response to constant external stimuli, without requiring spatiotemporal control of those stimuli (26). For example, soft robots made of light-, thermal-, or photothermal-responsive materials, such as hydrogels, polydimethylsiloxane (PDMS), and liquid crystal polymers or elastomers (LCPs or LCEs), have demonstrated autonomous linear motion when exposed to constant light sources or temperature (10-20). These robots often possess simple structural forms such as wavy or twisted ribbons, rods, helices, rings, and lattices (10-20). When placed in unstructured environments with obstacles, some self-rolling robots can perceive obstacles and autonomously redirect their motion (14-16, 19), enabling obstacle avoidance and even navigating simple obstacle courses and complex mazes through adaptive interactions with the obstacles (14, 19). Similarly, cantilever beams or fibers made of active materials, such as LCPs, LCEs, hydrogels, or bilayer LCE-PDMS composites, can undergo periodic self-oscillations under a constant light source (21-25), enabling flapping-based autonomous swimming and crawling (23, 25).

Significance

Topology and defect are crucial for autonomous soft mobile machines made of soft materials since they can dramatically change materials' responses. However, their interplay on autonomous motion remains largely unexplored. Here, we show that simply binding the two open ends of a twisted ribbon forms a closed-loop twisted ring topology alongside a defect at the binding site, generating distinct self-motion modes. As opposed to linear motion in self-rolling twisted ribbons under constant thermal actuation, the defected twisted ring exhibits three periodic coupled self-flip-spin-orbit motion with programmed circular and re-programmed non-circular paths in free and confined spaces, respectively, arising from the defect-induced rotational symmetry breaking in the twisted ring topology. This work has potential in autonomous robotic mapping of unstructured environments.

Author affiliations: aDepartment of Mechanical and Aerospace Engineering, North Carolina State University,

Author contributions: F.Q. and J.Y. designed research; F.Q., Y.L., Y.H., and J.Y. performed research; F.Q., Y.L., Y.H., Y.Z., H.Q., and J.Y. analyzed data; and F.Q., Y.L., Y.H., Y.Z., and J.Y. wrote the paper.

The authors declare no competing interest.

This article is a PNAS Direct Submission. R.Z. is a guest editor invited by the Editorial Board.

Copyright © 2024 the Author(s). Published by PNAS. This article is distributed under Creative Commons Attribution-NonCommercial-NoDerivatives License 4.0

¹To whom correspondence may be addressed. Email: jyin8@ncsu.edu.

This article contains supporting information online at https://www.pnas.org/lookup/suppl/doi:10.1073/pnas. 2312680121/-/DCSupplemental.

Published January 9, 2024.

Despite extensive research on autonomous linear and oscillating motions (10-25), periodic self-orbiting motion in autonomous soft mobile robots remains largely unexplored (see summary SI Appendix, Table S1), particularly in the context of periodic coupled spin-orbit motion commonly observed in nature, from atomic systems to celestial bodies. Within an atom, electrons spin and orbit around the nucleus. In the universe, planets spin and orbit around the Sun. Specially, the Earth exhibits both spinning and orbiting directions counterclockwise with different rotating periods (1 d vs. 1 y), while the Moon spins and orbits the Earth counterclockwise with the same periods (a month). More importantly, achieving periodic self-orbit motion beyond the conventional circular trajectory, for example, noncircular trajectories such as square and polygon shapes, or even irregular-shaped closed-loop trajectories, remains largely unexplored in autonomous soft mobile robots. Realizing these motions holds significant potential for autonomous and intelligent exploration in unstructured environments (1-3), as well as mapping (27-29), inspection (28), and structural health monitoring (30, 31) of unknown environments. These capabilities pose a grand challenge in the realm of autonomous soft mobile robotics yet to be accomplished (1-3).

Inspired by the periodic coupled spin-orbit motion observed in the universe, here, we report a celestial-like autonomous soft robot capable of periodic clockwise or counterclockwise spin-orbit motion under constant temperature or a constant light source. The robot takes a twisted ring topology with a defect, created by simply bonding the two ends of an open-end twisted ribbon made of thermal and photothermal-responsive LCEs (14) (Fig. 1A) with the defect located right at the binding site (red line in Fig. 1A). The twisted ring robot exhibits controllable, autonomous periodic synchronized flip-spin-orbit motions with circular and adaptive noncircular orbital paths in both a free space and confined spaces, respectively. Such controllable periodic self-orbiting motions are dramatically distinct from that of the reported open-end twisted ribbon, i.e., unidirectional linear motion in a free space and uncontrollable random motion in confined spaces (14), as well as that of the reported symmetric wavy LCE rings without chiral twists (16, 18), i.e., either sole inside-out self-flipping in place via snapping or linear motion after breaking the front-rear symmetric frictions (SI Appendix, Table S1). We validate experimentally and theoretically that it is the unique closed-loop twisted ring topology alongside the defect that leads to the distinct self-motions and underlying motion mechanisms from that of the open-end twisted ribbon (14).

Specially, the twisted ring robot exhibits three coupled self-rotatory motions: flipping around the circular centerline, spinning around the ring center, and orbiting along a circular path (Fig. 1B). Similar to the spin-orbiting motion of the Moon, it exhibits both identical spinning and orbiting directions and synchronized spinning and orbital periods, but differently with tunable clockwise and counterclockwise orbiting direction by the respective left- and right-handed twist chirality. The orbital periods and radius can be programmed by the geometry of the twisted ring, including ring radius, ribbon width, and twist density. Through combined analytical modeling and experiments, we find that the synchronized motion is driven by both the chiral twisted ring topology and the symmetry breaking of the tangential driving forces induced by the defect at the bonding site. Furthermore, we explore the robot's ability to perform re-programmed self-orbiting motions within confined spaces bounded by rigid walls, including both circular and non-circular orbits. The robot demonstrates intelligent mapping of the geometrical boundaries of diverse confined spaces with regular and irregular shapes, as well as the detection of structural damages along these confined spaces.

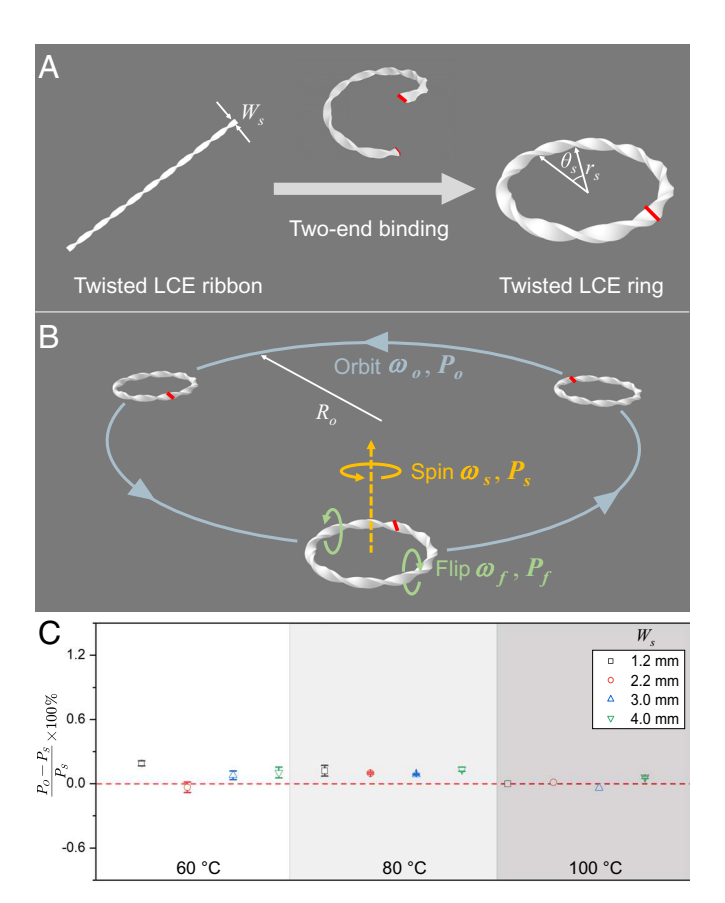


Fig. 1. Autonomous flip–spin–orbiting twisted LCE ring. (*A*) Schematics of constructing a twisted ring by simply binding the two ends of a prefabricated twisted LCE ribbon. The red lines denote the bonding site. W_s denotes the ribbon width. r_s and θ_s denote the ring radius and pitch angle, respectively. (B) Schematics of the exhibited coupled flipping, spinning, and orbiting motions around a circular path in response to constant temperature on a hot surface or a constant NIR light source $\omega_{\rm f}$, $\omega_{\rm s}$, and $\omega_{\rm o}$ denote the flipping, spinning, and orbiting angular velocities, respectively, with P_f , P_s , and P_o as the corresponding periods. R_o denotes the orbital radius. (C) The ratio of the difference between measured orbital period P_o and spinning period P_s to P_s for samples with different ribbon width in response to different surface temperatures.

Results

Autonomous Flip-Spin-Orbit Twisted LCE Ring. In constructing the twisted LCE ring, we follow a two-stage reaction method to synthesize the LCE materials (32) and then simply bond the two ends of the fabricated twisted LCE ribbon (14) without changing its twisting chirality (Fig. 1A and Materials and Methods). The geometry of the twisted ring can be characterized by the ribbon width W_s , ring radius r_s , and pitch angle θ_s that describes its twist density ($\theta = 2\pi/N$, where N is the number of twists).

When placed on a hot surface with a surface temperature Tover 60 °C, the twisted LCE ring exhibits celestial-like autonomous periodic coupled flip-spin-orbit motions (Fig. 1B, the optical images are shown in SI Appendix, Fig. S1). The coupled motions consist of continuous inside-out self-flipping around its circular centerline (Movie S1), self-spin around its ring center, and self-orbiting following a circular path (Movie S2). Similar flip-spin-orbit motions can be observed under remote nearinfrared (NIR) light, with a reversed outside-in self-flipping (Movie S3). The coupled motions can be described by the angular velocities $\boldsymbol{\omega}$ or equivalently period $P = 2\pi/\omega$ of flipping $(\boldsymbol{\omega_f} \text{ or } P_{\theta})$, spinning ($\boldsymbol{\omega}_{s}$ or P_{s}), and orbiting ($\boldsymbol{\omega}_{o}$ or P_{o}) motions, respectively, and the orbiting radius R_o . We find that $\boldsymbol{\omega_s}$ and $\boldsymbol{\omega_o}$ exhibit the same rotary direction (Fig. 1B) and magnitude (ω_s and ω_a)

regardless of the surface temperature and twisted ring geometry, i.e., the same orbital period shown in Fig. 1*C*. We note that ω_s and ω_a are over 250 times slower than ω_f (Fig. 2), i.e.,

$$\omega_s = \omega_o$$
 with $\omega_s = \omega_o \ll \omega_f$. [1]

The rotating direction is dependent of the twisted chirality (20). For a left-handed (right-handed) twisting ring, it spins and orbits clockwise (counterclockwise). We note that similar self-flipping was reported in a PDMS torus (12) on hot surfaces and wavy LCE rings on a hot surface (16, 18) or under a constant infrared light source (16), however, without observed both self-spinning and self-orbiting motion (12, 16, 18). Similar light-guided flip-spin motion was also reported in a bilayer LCE Mobius strip with defect-free designs (33), however, such a flip-spin motion is not autonomous since it needs external rotational controls of light sources with the absence of orbiting motion (33). We note that

the observed flip—spin—orbit motion is a result of the actuation of monodomain LCEs, rather than the sole thermal expansion of elastomers (SI Appendix, Fig. S2 and *Note S1*).

Next, we explore how the geometrical parameters and surface temperature T affect the coupled motions. Considering that $\omega_s = \omega_o \ll \omega_f$ in Eq. 1, we use the orbital period P_o and flipping angular velocity ω_f to describe the periodic motions. We find that P_o (similarly, ω_f) increases (decreases) with increasing W_s (Fig. 2 A and A), A, (Fig. 2 A and A), A, while decreasing (increasing) with A. In other words, a lower twist density and surface temperature, or a larger ribbon width and ring radius, result in a longer orbiting period and a slower flipping speed.

Among all the geometric parameters, W_s shows a more pronounced effect on both P_o and ω_f , especially at high temperatures of 120 °C, where P_o increases from ~8 to ~33 min (Fig. 2A) and ω_f decreases from ~4.5 to ~1.8 rad/s (Fig. 2D). However, surface

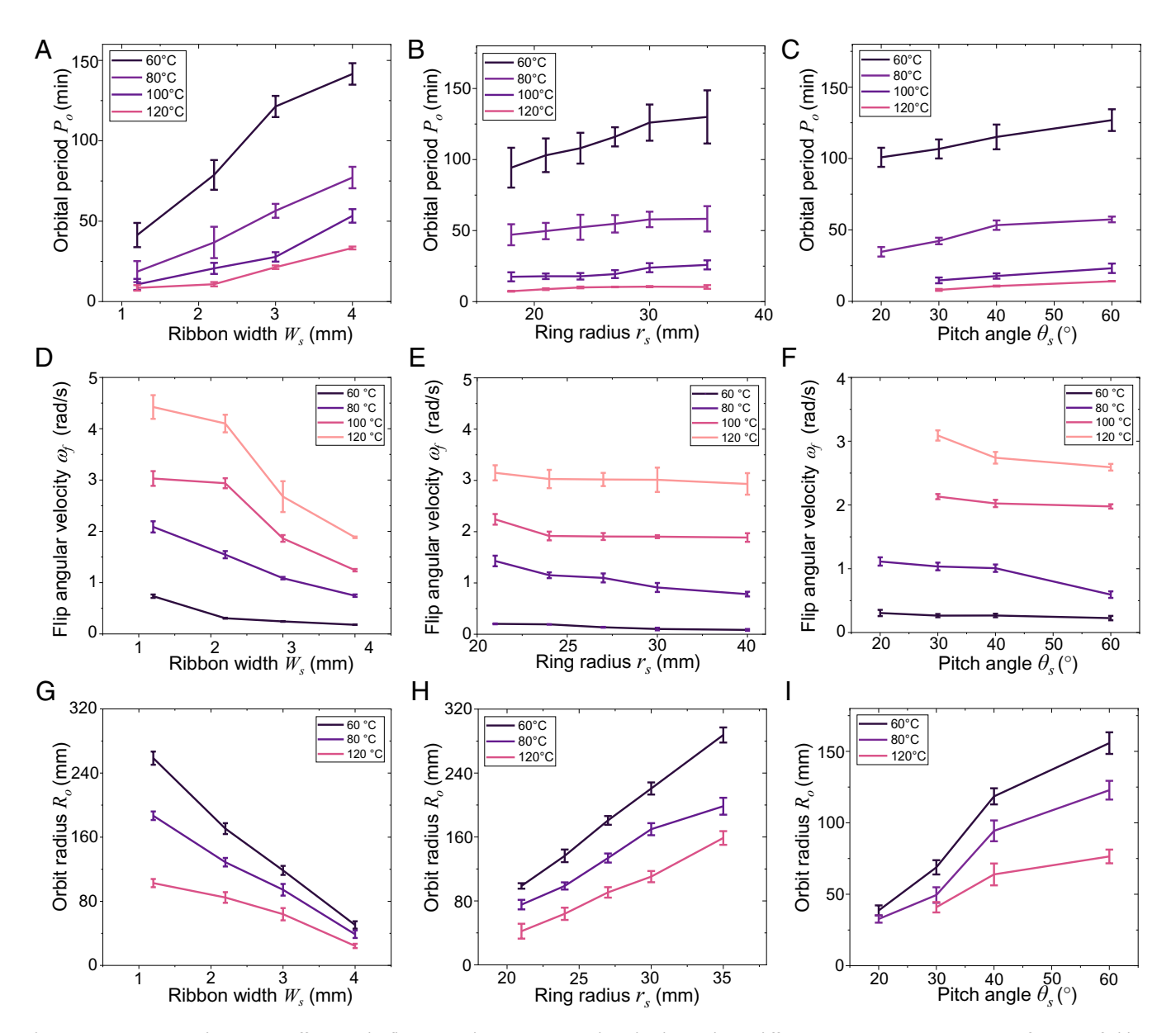


Fig. 2. Temperature and geometric effects on the flip–spin–orbit motion. (*A*–*C*) the orbital period P_o at different actuation temperatures as a function of ribbon width W_s (*A*), ring radius r_s (*B*), and pitch angle θ_s (*C*). (*D*–*F*) the flipping angular velocity ω_f at different actuation temperatures as a function of W_s (*B*), r_s (*E*), and θ_s (*F*). (*G*–*I*) the orbiting radius R_o at different actuation temperatures as a function of W_s (*G*), r_s (*H*), and θ_s (*I*). In (*A*), (*D*), and (*G*), r_s = 24 mm, θ_s = 40° (9 twists). In (*C*), (*F*), and (*I*), W_s = 3 mm, r_s = 24 mm.

temperature has the most prominent effect on both P_o and ω_f . As T increases from 60 to 120 °C, the average P_{θ} for different rings dramatically decreases from ~110 to ~10 min (Fig. 2 A-C), while the average ω_f increases from ~0.25 to ~3 rad/s (Fig. 2 *D–F*). Specially, for the twisted ring with smaller θ_s (more twists), e.g., $\theta_s = 20^\circ$, when $T \ge 100$ °C, it results in supercoiling (34) into an "8"-shape due to the higher stored twisting strain energy (Movie S4), which accounts for the missing data in Fig. 2 D and G. Similar supercoiling can be observed for all the twisted rings at a high temperature over 130 °C (SI Appendix, Fig. S3).

In contrast to the angular velocities, the orbiting radius R_o is significantly affected by both surface temperature and geometrical parameters (Fig. 2 G-I). R_o decreases with increasing T for all the studied twisted rings. However, the surface temperature shows a more pronounced effect for the rings with thinner ribbon width or larger ring radius or fewer twists. For example, as T rises from 60 to 120 °C, R_o decreases steeply from ~255 to ~100 mm for the twisted ring with $W_s = 1.2$ mm, over 2.5 times reduction, as opposed to the moderate decreases of R_a from ~50 to ~25 mm for the ring with $W_s = 4$ mm (Fig. 2G). Moreover, R_o shows a steep decrease with W_s (Fig. 2G) and a sharp increase with both r_s (Fig. 2H) and θ_s (Fig. 2I), especially at lower T of 60 and 80 °C. For example, when W_s increases from 1.2 to 4.0 mm, R_o decreases from ~255 to ~50 mm at 60 °C (Fig. 2G), while an increase in r_s from 21 to 35 mm results in an increase of R_o from ~100 to ~285 mm at 60 °C (Fig. 2H), which corresponds to an increase in R_o/r_s from ~5 to ~8.

Furthermore, based on the data of orbiting radius R_o and period P_o , the linear velocity of the orbiting ring v_o can be obtained in terms of $v_o = 2\pi R_o/P_o$. SI Appendix, Fig. S4 plots v_o as a function of ribbon width W_s , ring radius r_s , and pitch angle θ_s at different surface temperature T(SIAppendix). It shows that similar to ω_{β} v_a increases dramatically with T for the rings with thinner ribbon width or larger ring radius. Similar to R_o , v_o decreases dramatically with W_s while it increases with r_s at higher temperature, where W_s and r_s show a more prominent effect than θ_s on v_a (SI Appendix, Fig. S4).

Mechanisms Underpinning Flip-Spin-Orbit Motions. To gain further insight into the autonomous coupled motions observed in our experiments, we employ a combination of simplified theoretical modeling and experiments. Our investigations suggest that the observed coupled motions are attributed to a combination of factors, including temperature gradient-induced flipping moment in the LCE ring, the geometry of the twisting ring, and the breaking of symmetry at the two-end bonding spot, as discussed below.

Flip-Spin Motion. The twisted ring exhibits discrete thermal contact with the hot surface (Fig. 3 A and B), which results in temperature gradients across the ring height (SI Appendix, Figs. S5 and S6). This leads to the bottom contact regions of the ring shrinking, thereby engendering a moment M that drives the inside-out flipping (12, 13) (Inset of Fig. 3 C, SI Appendix, Note S1). As the ring selfflips, the initially heated regions on the bottom rotate to the top and become cooled down from natural convection. Despite the fast self-flipping angular velocity (e.g., ~4.5 rad/s in Fig. 2D), the dynamic thermal gradient is still preserved. Repeating such a cyclic heating and cooling process leads to the observed sustained self-slipping in experiments (SI Appendix, Fig. S7). The driving force \vec{F} can be defined as $\vec{F} = \partial M/\partial \alpha$, where α represents the flip angle (Fig. 3C). Due to the twisting of the ring, the tangential directions of the circular centerline I_c and the twisted boundaries

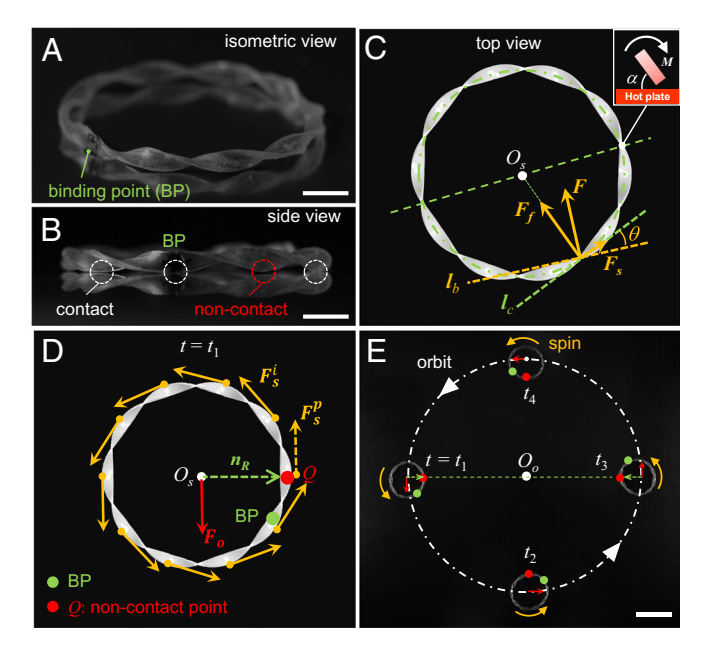


Fig. 3. Mechanism of the flip-spin-orbit motion. (A and B) Isometric and side view of an orbiting twisted ring on a hot surface (r_s = 24 mm, W_s = 2.2 mm, θ_s = 36° (10 twists), and right-handed chirality, T = 70 °C). White dashed circles highlight the contact points and the red dashed circle highlights the non-contact point (a small gap) right next to the BP. (Scale bar: 5 mm.) (C) Schematic of the driving forces for the motion in a twisted ring. I_c and I_b denote the tangential directions of the circular centerline and the twisted boundaries, respectively. F_s and F_f denote the spinning and flipping force components of the driving force F along I_c and I_b , respectively, with $F \perp I_b$, $F_s \parallel Ib$, and $F_f \perp I_c$. Inset shows the schematics of the driving moment M of the ring induced by the temperature gradient. (D) Schematic of the spinning driving forces F_s^i at the i^{th} contact point and the orbiting driving force $\emph{\textbf{F}}_{\emph{o}}$ of the orbiting twisted ring at the left position of (E). O_s and Q are the ring center and the noncontact point, respectively. n_R denotes the vector of O_sQ that points to the center of the orbiting circle O_0 in (E). (E) Overlapped optical images of the circular orbiting ring in (A) on a hot surface at four different time lapses located at the Top and Bottom, Left and Right of the orbit. Green and red dots highlight the BP and the non-contact point Q during orbiting, respectively (Scale bar: 5 cm.)

 $l_{\!\scriptscriptstyle h}$ do not align with each other, showing an intersecting angle hetathat changes along the twist boundary (Fig. 3C). As a result, the direction of F is perpendicular to I_b due to the evolving contact of the boundaries with the hot surfaces, i.e., $F \perp \mathit{l}_{b}$. Decomposing Falong l_c and the radial direction of the circular centerline generates the driving force for spinning F_s ($F_s \parallel I_c$) and flipping F_f ($F_f \perp I_c$) with their magnitudes of $F_s = F \sin \theta$ and $F_f = F \cos \theta$, respectively (Fig. 3C). Depending on its chirality, F_s leads to clockwise or counterclockwise spinning of the ring with left-handedness and right-handedness (Fig. 3C), respectively, which is consistent with the experiments. The relationship between ω_s and ω_f can be given by (see details in SI Appendix, Note S1)

$$\omega_{s} = \cot\theta \omega_{f}. \tag{2}$$

At the boundary contact, we have a small angle mismatch of θ < 1° for the studied twisted rings. Thus, it renders a much faster flipping than spinning observed in the experiments.

Spin-Orbit Motion. The orbiting motion is attributed to the force balance breaking induced by the defect at the two-end bonding site, where the twisted mesogen alignments along the centerline become discontinuous. For a perfect defect-free twisted ring (Fig. 3C) with N twists, all the discrete twisted boundaries remain contact with the hot surface during motion, and we have $\sum_{i=1}^{N} \boldsymbol{F}_{s}^{i} = \mathbf{0}$ due to its closed-loop geometry, where \boldsymbol{F}_{s}^{i} is

the spinning driving force at the i^{th} twisted boundary with its direction tangential to the circular centerline (Fig. 3D). However, we observe that for the two-end bonded twisted ring, all of the discrete twisted boundaries are in contact with the hot surface during motion except for the one denoted as F_s^p (Fig. 3D). Such a non-contact point is located right next to the binding point (BP), as evidenced by the small gap shown in Fig. 3*B* induced by the periodic slight lift-up during spinning motion (Movie S5). We note that the relative locations between the non-contact point and the BP can change depending on the geometry of the twisted ring. As a result, it breaks the balance among F_{s}^{i} , generating a net force $\sum_{i=1}^{N} F_{s}^{i} = -F_{s}^{p} = F_{o}$ that drives the orbiting of the twisted ring along the same spinning direction (Fig. 3 D and E and SI Appendix, Fig. S8 and Note S2).

The spinning and orbiting dynamics of the ring are intricately linked, as the location of the defect (BP) undergoes circular motion along the circular centerline while the ring self-spins (Fig. 3*E*). Consequently, the direction of the net force acting on the ring undergoes rotation in tandem with the spinning defect. Remarkably, the ring completes a full circle of self-spinning right before the defect returns to its original position, leading to the completion of a full circle in the orbiting motion (Fig. 3E and SI Appendix, Fig. S8 and Note S2). Thus, the synchronized spinning and orbiting dynamics underpin the observed identical periods in both motions.

The net force also governs the direction of the ring's orbit. Specifically, a vector \mathbf{n}_{R} connecting from the ring's center O_{s} to the non-contact point Q (Fig. 3D) points to the center of the orbiting circle O_o (Fig. 3E). As a result, the orbiting direction n_o , which denotes the tangential direction of the orbiting circle, remains perpendicular to n_R throughout the orbiting motion, i.e., $n_o \perp n_R$. This finding is consistent with the experimental observations depicted in Fig. 3E.

Effects of Temperature and Geometry on Flip-Spin-Orbit Motion. To qualitatively understand the surface temperature and geometrical parameters on the flip-spin-orbit motions, we develop a simplified dynamics model on predicting the flipping angular velocity ω_f (see more details in SI Appendix, Note S3), which scales as:

$$\omega_f \propto \frac{N\kappa_s \alpha \Delta TL}{\operatorname{arcsinh}(NW_s \kappa_s)},$$
 [3]

where α and L denote the thermal expansion coefficient and the sample length, respectively, $\Delta T = T - T_{ambient}$ ($T_{ambient}$ is the ambient temperature) is the temperature difference, $\kappa_s = 1/r_s$ is the curvature of the ring, and the function arcsinh is monotonic. SI Appendix, Fig. S9 shows the comparison of ω_f between the analytical model and experimental data as a function of ribbon width W_s , ring radius r_s , and pitch number N at varying actuation temperatures T. The model shows that ω_f diminishes with increasing W_s and r_s . On the other hand, ω_f rises with a higher pitch number N. Compared to these geometric parameters, the surface temperature T shows a more notable effect, where ω_f surges with T, which are consistent with the experiments (Fig. 2 A-F and SI Appendix, Fig. S9).

The orbiting radius R_{ρ} can be expressed as in terms of the centripetal force (SI Appendix, Note S3)

$$R_o = \frac{gC_f}{\omega_o^2},\tag{4}$$

where C_f is the dynamic coefficient of friction and g is the gravitational constant. Eq. 4 shows that R_a is inversely proportional to the self-spinning frequency, ω_o . Accordingly, R_o increases as ω_o decreases, and since ω_o is linearly proportional to the self-flipping frequency, ω_f , as described by Eqs. 1–3, decreasing ω_f will also lead to an increase in R_o . This is consistent with the experimental observations presented in Fig. 2. Similarly, as indicated by Eq. 3, increasing r_s and θ_s or decreasing W_s and T will result in a reduced ω_f and hence a decreased ω_o , leading to an increase in R_o . Notably, since R_o is inversely proportional to ω_o^2 , geometrical parameters and surface temperature will present a more prominent effect on R_o than on ω_f , which is also consistent with the experiments.

Autonomous Exploration of Confined Spaces. Next, we explore leveraging the observed autonomous flip-spin-orbit motion of the twisted rings in free space as a soft robot for programmed autonomous periodic motions in different confined spaces on hot surfaces (90 °C), as well as its applications in intelligent mapping and health monitoring of its boundary shapes. The confined spaces are constructed from enclosed spaces with different geometrically shaped wooden walls.

Upon randomly placing the left-handed twist ring (Fig. 4A and Movie S6) with its radius R smaller than its free-space orbiting radius R_a (i.e., $R \le R_a$) inside a circular confine space, we observe that the soft robot first self-move to the wall and then exhibit a periodic self-orbiting motion along the inner boundary of the circular wall, demonstrating a similar flip-spin-orbit motion with identical spinning and orbiting periods. However, due to the side interaction (i.e., friction) of the ring with the wall, the orbiting direction n_o does not adhere to the rule in Eq. 3 with $n_o \perp n_R$. While $R \leq R_o$ serves as a sufficient condition for self-orbiting around the confined circular wall, it is not a necessary condition as the ring-wall interaction and friction play an important role.

We further explore the self-orbiting behavior of the twist ring robot in non-circular-shaped confined spaces, such as a square and equilateral triangular shape, as shown in Fig. 4B (Movie S7) and Fig. 4C (Movie S8), respectively. We constrain the projection of the side length of both shapes to the horizontal direction (L_b) and the vertical direction (L_v) to be $L_h \le R_o$ and $L_v \le R_o$. However, such constraints only represent a sufficient condition. Nevertheless, the soft robot can self-orbit periodically around both square and triangular-shaped walls after one or two trials of orbiting motions. We observe that its orbiting motions are very different from the coupled flip-spin-orbit motion observed in free spaces and confined circular spaces. When it contacts the straight side wall, the twist ring robot moves linearly along the wall irrespective of its orientation. Interestingly, the ring only self-flips and does not self-spin around its circular centerline during its linear motion, as indicated by the non-spinning motion of the defect (Fig. 4 B, ii, Fig. 4 C, iii, SI Appendix, Fig. S10, and Movies S7 and S8). The absence of self-spinning motion results from the suppression of its spinning driving force F_s by the friction force f from the side wall, where F_s and f are aligned with opposite directions along the

However, whenever it moves to a corner, it starts to self-spin and self-turn and then transits to linear motion, accomplished by the cessation of self-spinning with only flipping (Fig. 4 B, iii, Fig. 4 C, ii, SI Appendix, Fig. S10, and Movies S7 and S8). This behavior results from the spinning driving moment generated by the two angled spinning driving forces against the angled walls (SI Appendix, Fig. S11 and *Note S4*). After one complete cycle of orbiting, we observe that the twist ring returns to its original position when it first meets the side wall, as indicated by the identical defect

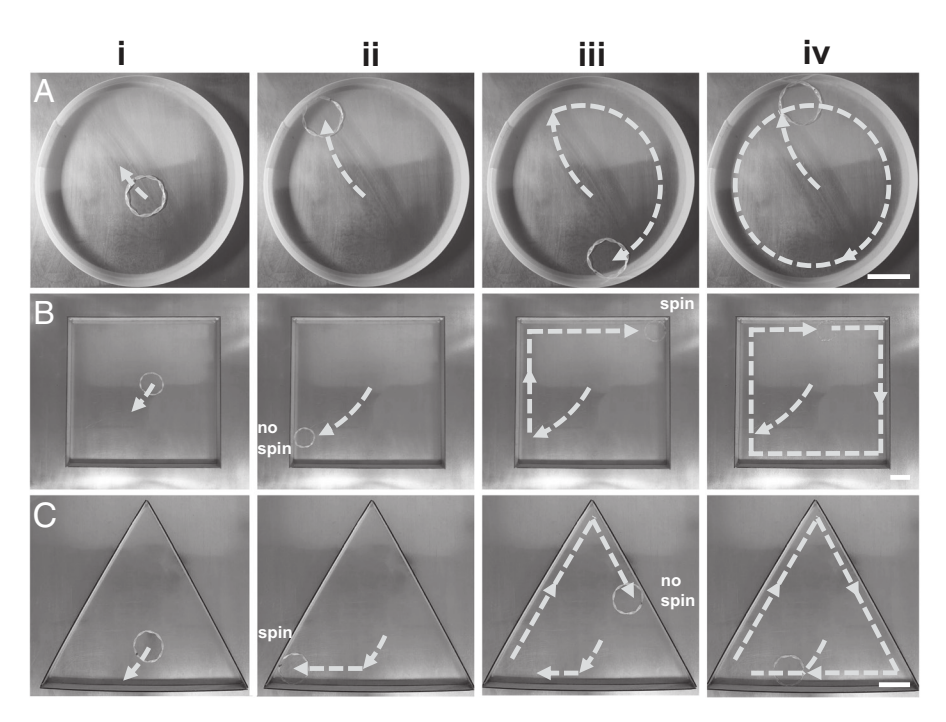


Fig. 4. Autonomous periodic orbiting around circular and non-circular paths. (*A–C*) Periodic orbiting motions of a randomly placed twisted ring robot ($r_s = 24$ mm, $W_s = 3$ mm, $\theta_s = 40^\circ$ (9 twists, and left-handed chirality) in circular (*A*), square (*B*), and triangular (*C*) confined spaces by plastic sheets or wooden walls on hot surfaces (90 °C). The dashed curves show the tracked motion trajectories. (Scale bar: 5 cm.)

positions before and after orbiting, indicating that the same spinning and orbiting periods still hold true in confined spaces.

Intelligent Mapping and Structural Health Monitoring of Confined Spaces. Expanding on its self-orbiting capability, we further explore its potential application in intelligently mapping the boundary shapes of enclosed confined spaces. To demonstrate this, we coat the robot's body with fluorescent powder and place it in a priori unknown confined space in complete darkness (Fig. 5 A, i and Movie S9). Tracking the glowing orbiting trajectory of the robot reveals a pentagon-shaped profile, which matches the shape of the boundary walls (Fig. 5 A, ii and iii). Not limited to convex shapes like squares, triangles, and pentagons with interior angles less than 180°, we also explore the robot's potential to map concave shapes with an interior angle greater than 180°, such as the Chinese character ""-shaped confined space shown in Fig. 5B (Movie S10). The robot effectively captures the left part of the boundary shape using both linear motion at straight boundaries and self-turning at convex corners (Fig. 5 B, i). However, when self-navigating to the concave corner, it transits to free-space circular orbiting motion due to the loss of contact (SI Appendix, Fig. S11 and Note S4). The robot then quickly moves to the bottom wall and repeats this hybrid linear-arc orbiting motion, represented by the green dotted trajectory U_L in Fig. 5 B, i. To cover the entire boundary shape, we use another twist ring robot with opposite handedness, i.e., right-handed, to capture the other half of the boundary, as shown by the orange color dotted trajectory U_R in Fig. 5 B, ii. Fig. 5 B, iii shows the union of the two sets of the trajectories, i.e., $U_L \cup U_R$, which provides an approximate profile of the entire boundary shape (Fig. 5 B, iv). We note that the detection resolution of the geometric boundaries of a confined space is determined by the orbiting radius of the ring. To achieve higher detection resolution, i.e., confined spaces with smaller sizes, as indicated by Eqs. 3 and 4, a smaller ring size with relatively wider ribbon width or more twists is preferred.

However, it is challenging for small-sized rings to sustain sufficient thermal gradient, making them homogenously heated and tend to supercoil, losing its orbiting mobility.

Furthermore, we explore its ability of detecting structural damages in the boundary of enclosed confined spaces for potential applications in structural health monitoring. Fig. 5C shows one example of the same enclosed square-shaped confined space in Fig. 4B but with one gap as structural damage in one side wall. Depending on the relative gap size l_{σ} to the ring diameter d_{s} , the soft robot is capable of either still self-orbiting around the boundary but with an abrupt change in its tracked trajectory when $l_{\sigma} \le$ d_s (Fig. 5 C, i and ii and Movie S11), i.e., a non-continuous slight jump at the gap site, or self-escaping from the confined space when $l_{\varphi} > d_s$ due to the contact loss at the gap (Fig. 5 C, iii and iv and Movie S12). These signs indicate the damage and its approximate damage size in the enclosed wall. For a confined space with more damages in other side walls, a combination of left-handed and right-handed twisted rings could be utilized to detect multiple damage sites.

Lastly, we demonstrate the versatility of the twist ring robot by programming it to exhibit autonomous reciprocating motion in an open-end channeled space, as depicted in Fig. 5D (Movie S13). The channel width w and length L are set to 50 mm and 600 mm, respectively, with w slightly wider than the ring diameter of 45 mm and L much larger than the free-space orbiting diameter $2R_o = 120$ mm. The robot moves back and forth within the channel by utilizing the coupled flip-spin-orbit motion and the interactions with both channel walls. Specifically, it initially moves linearly to the right, then turns around and moves linearly to the left, followed by another turnaround at the left end. This periodic back-and-forth motion is attributed to the spatiotemporal variation of the driving force $\sum_{i=1}^{N} F_{s}^{i} = -F_{s}^{p}$, coupled with the sidewall friction from both channel walls (SI Appendix, Fig. S11 and Note S4). Interestingly, we find that the distance between two turnaround points is approximately equal to $2R_{o}$. Thus, the original circular orbiting motion of

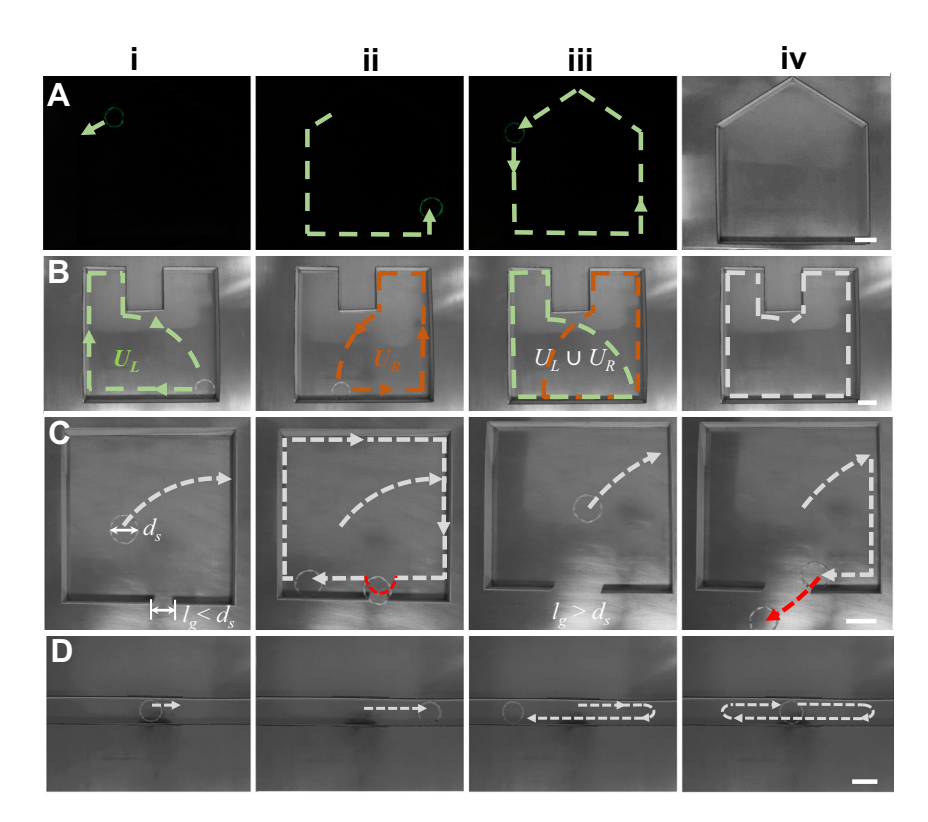


Fig. 5. Intelligent mapping and damage detections of confined spaces. (A) Mapping of the boundary shape of a priori unknown confined space in complete darkness via autonomous periodic orbiting of the twisted ring robot. The robot is coated with fluorescent powder to track its moving trajectory highlighted by the green dashed lines in (i-iii). (iv) shows the image of the pentagon-shaped confined space. (B) Boundary shape mapping of a concave-shaped confined space using two orbiting twisted ring robots with right-handed (i) and left-handed chirality (ii). (i), (ii), and (iii) show the two tracked trajectories (U_L and U_R) and the union of two sets of U_L and U_R (i.e., $U_L \cup U_R$), respectively. (iv) shows the tracked trajectory after removing the intersection of the two sets that matches the concave boundary shape of the confined space. (C) Orbiting motions in square-shaped confined spaces with damages (a gap) in the bottom side walls with smaller (i and ii) and larger (iii and iv) gap size l_g than the ring diameter d_{sr} respectively. $l_g = 25$ mm in (i and ii) and $l_g = 80$ mm in (iii and iv) with $d_s = 48$ mm. The white color dashed curves and lines show the motion trajectories. Red curves denote the motion trajectories when meeting the gaps. (*D*) Autonomous one-dimensional (1D) reciprocating motion in an open-end channeled confined space. All the demos are on hot surfaces (90 °C). In (*A*–*C*), r_s = 24 mm, W_s = 3 mm, θ_s = 40° (9 twists), and right-handed chirality in (*A*) and (*B*, *ii*) and left-handed chirality in (*B*, *i*) and (*C*). In (*D*), r_s = 24 mm, W_s = 3 mm, θ_s = 30° (12 twists), and left-handed chirality. (Scale bar: 5 cm.)

the twist ring is converted into a reciprocating motion through this one-dimensional confined channel.

Discussions

We demonstrated leveraging a defected, closed-loop twisted ring topology for a thermally actuated self-orbiting LCE soft robot. It can autonomously and periodically orbit in both free and confined spaces with programmed circular and reprogrammed non-circular trajectories and period via coupled flip-spin-orbit motions. The flip-spin motion is attributed to the closed-loop twisted ring topology, while the orbiting motion arises from the defect at the twoend binding site that breaks the balance of the spinning driving forces due to the loss of contact. Through the adaptive contact interactions between the flip-spin-orbit soft robot and the boundary walls, it can either periodically self-orbit along the boundaries of confined spaces with both concave and convex shapes, or periodically self-oscillate along a straight line in an open-end channeled space, by means of spontaneously and adaptively enabling or disabling the spinning motion. The self-orbiting single or multisoft robots are capable of mapping the boundary's geometric shapes of priori unknown confined spaces and detecting the damages of their boundary.

All these unprecedented autonomous periodic motions in both free and confined spaces are attributed to the synergy between the closed-loop twisted ring topology and the binding defect, which is absent in previous studies on self-motion structures with either open-end or closed-loop geometries (10-19). Topologically, the

twisted ring is dramatically distinct from the open-end twisted ribbon (14). After binding and bending into a twisted ring, it offers several unique benefits compared to the open-end twisted ribbon: 1) the closed-loop twisted topology prevents the untwisting in the open-end twisted ribbon, preserving a constant number of twists for stable spinning. 2) The defect breaks the rotational symmetry of the twisted ring during spinning motion due to the loss of contact, which enables the coupled spinning-orbiting motion. Without the defect, in principle, the ring can only flip and spin and cannot orbit. 3) The closed-loop twisted topology enables handedness-governed spin-orbit motion. The clockwise or counterclockwise spin or orbit depends on the handedness, while both the linear motion and random motion in the open-end ribbon are independent of its handedness (14).

Moreover, for self-motion structures in a closed-loop ring topology, the absence of either twisted features or defects leads to distinct motions from the adaptive flip-spin-orbit motion in this work. For example, a twist-free PDMS or nylon fiber-based torus with a binding defect only exhibits self-flipping motion in place on hot surfaces (12). Similar sole self-flipping motion is also reported in a 2D wavy LCE ring on a hot plate composed of multiple connected pre-curved non-twisted cylindrical fibers with multiple binding defects (18), as well as in a defect-free 3D wavy LCE dancing ring on hot surfaces or under constant NIR light (16). The absence of the coupled spin-orbit motion in these ring structures is due to their highly symmetric ring geometry. Despite the presence of defects, the symmetric ring geometry without chiral twists (16, 18) cannot generate a similar tangential driving force for self-spinning to the twisted ring (Fig. 3 *C–E*). To generate a continuous flip–spin motion in a defect-free bilayer LCE Mobius strip, it requires spatiotemporal control of the NRI light along the ring (33). Furthermore, we observe that the size and number of the defects in the twisted LCE ring can also change its orbiting motion. For example, a larger defect size could result in a smaller orbital radius (*SI Appendix*, Fig. S12). The orbiting motions in the twisted rings with multiple defects become more complex due to the interplay of the multiple defects (*SI Appendix*, Fig. S13). Generally, as the number of defects increases, the twisted rings become more unstable and tend to supercoil into "8" shapes even at lower actuation temperature (*SI Appendix*, Fig. S13). The effect of the number of binding defects on the spin-orbiting motion of the twisted ring will be explored in the future.

The self-orbiting soft robot and swarms can find potential applications in intelligent exploration, mapping, and health monitoring of priori unknown environments and confined spaces (27–31).

Materials and Methods

The twisted LCE rings were fabricated by gluing the two ends of a twisted LCE ribbon that was manufactured by following the two-stage reaction method in our previous work (14). Two g of 1,4-Bis-[4-(3-acryloyloxypropyloxy) benzoyloxy]-2-methylbenzene (RM257) (Wilshire Company, 95%) was fully dissolved into 0.7 g of toluene (Sigma Aldrich, 99.8%) at 85 °C under magnetic stirring. Then, 0.012 g of (2-hydroxyethoxy)-2-methylpropiophenone (HHMP; Sigma-Aldrich, 98%), 0.42 g of 2,2'-(ethylenedioxy) diethanethiol (EDDET, Sigma Aldrich, 95%), and 0.19 g of pentaerythritol tetrakis (3-mercaptopropionate) (PETMP, Sigma

- 1. C. Majidi, Soft-matter engineering for soft robotics. Adv. Mater. Technol. 4, 1800477 (2019).
- 2. S. I. Rich, R. J. Wood, C. Majidi, Untethered soft robotics. Nat. Electron. 1, 102-112 (2018).
- J. Pinskier, D. Howard, From bioinspiration to computer generation: Developments in autonomous soft robot design. Adv. Intell. Syst. 4, 2100086 (2022).
- L. Hines, K. Petersen, G. Z. Lum, M. Sitti, Soft actuators for small-scale robotics. Adv. Mater. 29, 1603483 (2017).
- Y. Y. Xiao, Z. C. Jiang, Y. Zhao, Liquid crystal polymer-based soft robots. Adv. Intell. Syst. 2, 2000148 (2020).
- Z. Shen, F. Chen, X. Zhu, K. T. Yong, G. Gu, Stimuli-responsive functional materials for soft robotics. J. Mater. Chem. B 8, 8972–8991 (2020).
- Y. Zhao et al., Stimuli-responsive polymers for soft robotics. Ann. Rev. Control Rob. Auton. Syst. 5, 515–545 (2022).
- Y. Chi et al., Bistable and multistable actuators for soft robots: Structures, materials, and functionalities. Adv. Mater. 34, 2110384 (2022).
- Y. Chi, Y. Zhao, Y. Hong, Y. Li, J. Yin, A perspective on miniature soft robotics: Actuation, fabrication, control, and applications. Adv. Intell. Syst. 2300063 (2023).
- A. H. Gelebart et al., Making waves in a photoactive polymer film. Nature 546, 632–636 (2017).
- C. Ahn, K. Li, S. Cai, Light or thermally powered autonomous rolling of an elastomer rod. ACS Appl Mater. Interface 10, 25689-25696 (2018).
- 12. A. Baumann et al., Motorizing fibres with geometric zero-energy modes. Nat. Mater. 17, 523–527 (2018).
- 13. A. Bazir, A. Baumann, F. Ziebert, I. M. Kulić, Dynamics of fiberboids. Soft Matter 16, 5210–5223 (2020).
- Y. Zhao et al., Twisting for soft intelligent autonomous robot in unstructured environments. Proc. Natl. Acad. Sci. U.S.A. 119, e2200265119 (2022).
- F. Zhai et al., 4D-printed untethered self-propelling soft robot with tactile perception: Rolling, racing, and exploring. Matter 4, 3313–3326 (2021).
- Y. Zhao et al., Self-sustained snapping drives autonomous dancing and motion in free-standing wavy rings. Adv. Mater. 35, 2207372 (2023).
- 17. J. J. Wie, M. R. Shankar, T. J. White, Photomotility of polymers. Nat. Commun. 7, 13260 (2016).
- D. S. Kim, Y. J. Lee, Y. B. Kim, Y. Wang, S. Yang, Autonomous, untethered gait-like synchronization of lobed loops made from liquid crystal elastomer fibers via spontaneous snap-through. Sci. Adv. 9, eadh5107 (2023).

Aldrich, 95%) were then added to the solution. The solution was stirred at 85 °C for 20 min. After cooling down to room temperature, 0.006 g of catalyst, dipropylamine (DPA; Sigma-Aldrich, 98%) was added and stirred at room temperature for 3 min. Then, the solution was poured in the mold and let stand overnight for fully reaction. The sample is left in the mold and dried at 75 °C for 24 h. The twisted LCE ribbon was obtained by first stretching the dried ribbon to about 150% of its initial length and then twisted and exposed under UV irradiation for 10 min to finish the crosslinker process. The two ends of the twisted ribbon were bonded using UV epoxy resin (Limino) for 3 min under 395 nm UV flashlight to achieve the twisted LCE ring (the defect shape and size are shown in Fig. 3 A and B). The two ends were glued using UV adhesive resin with compatible geometrical connections to preserve the twisting chirality. The ribbon was stretched to 150% of its initial length and twisted for UV curing. The spin-flip-orbiting motion of all the twisted LCE rings was performed on a 18"×24" hotplate (McMaster-Carr) with aluminum heating surface and tracked by a DSLR camera (Sony ILCE7M3). Metal polishing method was applied to the aluminum surface to ensure uniform surface friction. All the motions were measured in the steady states (SI Appendix, Fig. S14) with at least four samples for each data point. The error bar stands for the SD of the measurements. The BP was marked with colored markers to track the motion. The infrared images were taken with an infrared camera (FLIR A655sc). The enclosed walls in the confined spaces were created by gluing thin wood bars cut by a laser cuter (Epilog Laser Mini) to construct the studied different shaped boundaries. The twisted ring was coated with lime-color fluorescent powder that emits glows after being charged under sunlight to track its motion in a dark room.

Data, Materials, and Software Availability. All study data are included in the article and/or supporting information.

ACKNOWLEDGMENTS. J.Y. acknowledges the funding support from NSF, award # CMMI-2005374 and CMMI-2126072.

- Y. Zhao et al., Physically intelligent autonomous soft robotic maze escaper. Sci. Adv. 9, eadi3254 (2023).
- L. Yin et al., Chiral liquid crystalline elastomer for twisting motion without preset alignment of mesogens. ACS Macro Lett. 10, 690-696 (2021).
- 21. H. Zeng et al., Light-fuelled freestyle self-oscillators. Nat. Commun. 10, 5057 (2019).
- 22. Q. He et al., Electrospun liquid crystal elastomer microfiber actuator. Sci. Rob. 6, eabi9704 (2021).
- Y. Zhao et al., Soft phototactic swimmer based on self-sustained hydrogel oscillator. Sci. Rob. 4, eaax7112 (2019).
- R. Yoshida, T. Ueki, Evolution of self-oscillating polymer gels as autonomous polymer systems. NPG Asia Mater. 6, e107 (2014).
- Y. Zhao et al., Sunlight-powered self-excited oscillators for sustainable autonomous soft robotics. Sci. Rob. 8, eadf4753 (2023).
- Y. Kim, X. Zhao, Magnetic soft materials and robots. Chem. Rev. 122, 5317–5364 (2022).
- S. Thrun, W. Burgard, D. Fox, "A real-time algorithm for mobile robot mapping with applications to multi-robot and 3D mapping" in Proceedings 2000 ICRA. Millennium Conference. IEEE International Conference on Robotics and Automation. Symposia Proceedings (IEEE, San Francisco, CA, 2000), pp. 321-328.
- H. J. S. Feder, J. J. Leonard, C. M. Smith, Adaptive mobile robot navigation and mapping. Int. J. Rob Res. 18, 650-668 (1999).
- F. Amigoni, "Experimental evaluation of some exploration strategies for mobile robots" in 2008 IEEE International Conference on Robotics and Automation (IEEE, Pasadena, CA, 2008), pp. 2818–2823.
- Y. Tian, C. Chen, K. Sagoe-Crentsil, J. Zhang, W. Duan, Intelligent robotic systems for structural health monitoring: Applications and future trends. *Autom. Constr.* 139, 104273 (2022).
- R. G. Lins, S. N. Givigi, "Autonomous robot system architecture for automation of structural health monitoring" in 2016 Annual IEEE Systems Conference (SysCon) (IEEE, Orlando, FL, 2016), pp. 1–7.
- C. M. Yakacki et al., Tailorable and programmable liquid-crystalline elastomers using a two-stage thiol-acrylate reaction. RSC Adv. 5, 18997–19001 (2015).
- Z. Z. Nie et al., Light-driven continuous rotating Mobius strip actuators. Nat. Commun. 12, 2334 (2021).
- A. Clement et al., Complexity from simplicity: Confinement directs morphogenesis and motility in nematic polymers. Extreme Mech. Lett. 47, 101362 (2021).